*Physics – Uspekhi* **59** (9) 829 – 845 (2016) 

***REVIEWS OF TOPICAL PROBLEMS***

PACS numbers: 68.35.Np, **87.10.– e**, 87.85.jf

# Biological microstructures with high adhesion and friction. Numerical approach

V L Popov, A E Filippov, S N Gorb

DOI: 10.3367/UFNe.2016.01.037677

## Contents



**Abstract. Over the course of biological evolution, many classes of living creatures have developed highly effective adhesive mechanisms that allow them to attach to various kinds of surfaces having different physical natures and topographies. The most famous instance of this is the gecko pad, but many similar examples are found in animals of different sizes and evolutionary lineages. In recent decades, such adhesive structures have become the objects of intensive theoretical and experimental studies, partly due to research aimed at developing and producing artificial surfaces with similar adhesive properties. Here, we present a review of research on biological structures with high adhesion and high friction. We focus our attention on one particular class of such structures: systems with elastic fibers interacting with rough surfaces. Other structurally similar systems are discussed as well.**

**Keywords:** adhesion, friction, fibrous structures, gradient materials, bionics

**V L Popov** Technische Universität Berlin, Institut für Mechanik, FG Systemdynamik und Reibungsphysik, Sekr. C8-4, Raum M 122, Straße des 17. Juni 135, 10623 Berlin, Germany
E-mail: v.popov@tu-berlin.de
**A E Filippov** A A Galkin Donetsk Institute for Physics and Engineering, National Academy of Sciences of Ukraine,
R Luxemburg str. 72, 83114 Donetsk, Ukraine
E-mail: filippov_ae@yahoo.com
**S N Gorb** Department Functional Morphology and Biomechanics, Zoological Institute of the University of Kiel,
Am Botanischen Garten 1–9, D-24098 Kiel, Germany
E-mail: sgorb@zoologie.uni-kiel.de

Received 8 November 2015
*Uspekhi Fizicheskikh Nauk* **186** (9) 913 – 931 (2016)
DOI: 10.3367/UFNr.2016.01.037677
Translated by Yu V Morozov; edited by A Radzig

## 1. Introduction

Over the last two decades, considerable attention of the scientific community has been drawn to dry adhesion inherent in certain biological objects and manifested on micro- and nanoscales [1–7]. Important experimental and theoretical studies have been carried out to gain a deeper insight into this phenomenon.

One of the most famous objects of such research is the gecko pads, which has been thoroughly investigated in many laboratories. It was revealed, in particular, that the footpads of the gecko are covered with an array of microscopic hair-like bristles (setae), each ending in a thin (5–10 nm) leaf-like plate (spatula) so small that it conforms to the surface roughness practically at the molecular level.

From the very beginning, it was supposed that the setal structure promotes adhesion and its control. The existence of natural systems capable of increasing the overall contact area and adhesion to such an extent that animals can literally walk on walls and ceilings gave impetus to nanotechnology research and designing analogous artificial systems. Considerable progress has been achieved in the fabrication of polymeric adhesive surfaces mimicking the structure of the gecko's footpad setae and spatulae [6–8]. The properties of certain artificial systems are very similar to those of natural ones. Some of them are made of relatively stiff materials, such as nanotubes or microelectromechanically produced organo-polymeric nanorods (so-called organorods) [9, 10], which exhibit good adhesive properties, too.

A natural footpad possessing adhesive properties has a very complicated structure, and its adhesion ability originates from a combination of many contributions covering different scales [4, 11–13]. It has developed over the course of biological evolution by natural selection and appears to be highly optimized, even if it probably retains random traits, sort of rudiments, of a structure that continues to mature spontaneously up to the present time. For this reason, there is no need to reproduce it precisely: suffice it to adopt the principle of action of fibers or processes in order to create artificial structures like nanotubes or elastic mushroom-shaped structures, making them as manufacturable as possible. Practical realization of adhesive structures implies the necessity of numerical simulation to find the optimal relationship among system parameters [14–16]. Although it is much easier to model artificial structures than mesoscopic natural objects, they remain complicated multibody systems moving in all three dimensions.

The development of artificial adhesive systems entails the analysis of structures and properties incorporated in the design of living creatures by nature itself. It is known, for instance, that the formation of contact between insect adhesive footpads and various substrates is due to the footpad's ability to conform to different topographic patterns, which is further strengthened by the presence of specific micro- and nanostructures on the feet of these arthropods [17–21]. Moreover, the trapping of cracks in adhesive systems with multiple contacts provides additional advantages as they attach to rough surfaces [22]. The hierarchical organization of footpad structures in insects, just as in geckos, enables the formation of multiple contacts and essentially contributes to the enhancement of overall contact length and total peeling time [23].

It has recently been shown in Ref. [24] that thin-film-like spatular tips in setal attachment pads are responsible for the maximum increase in the contact area under the action of an applied shear force without slippage along the contact. This suggests the importance of elasticity of the material of setal tips for the formation of contact zones in adhesive footpads. Elastic materials are capable of forming large contact areas under a minimal load. On the other hand, lengthy structures from very soft materials are characterized by low mechanical stability [25]: insect adhesive setae from such materials may twist and collapse, giving rise to so-called clusterization (gluing) [26, 27]. Clustering markedly deteriorates the functional properties of adhesive contacts and may contribute to their disappearance in the absence of proper adaptation. In other words, adhesive structures of insects exemplify a typical case of the optimization problem solution over the course of biological evolution by the formation of thickness and mechanical property gradients. The thickness gradients in various adhesive setae of insects are well known owing to numerous electron microscopic studies [17].

A recent comprehensive study on the structure and mechanical properties of the tarsal setae material of the ladybird beetle (*Coccinella septempunctata*) has demonstrated the presence of a thickness gradient in each separate seta [28]. Young's modulus of ladybird setae measured by atomic force microscopy (AFM) was found to vary from 1.2 MPa at their tips to 6.8 GPa at the bases [28]. Setal tips were shown to contain a large concentration of the rubber-like protein resilin [29, 30], whereas their bases are made up largely of hardened cuticle. A previous analysis made by contact laser scanning microscopy (CLSM) also revealed high concentrations of a rubber-like protein in the setal tips [28, 31, 32]. Both central and basal parts of the setae preferentially autofluoresce in blue, yellow, and red due to the presence of other (presumably hardened) proteins, most probably resilin (blue) and sclerotized chitin (yellow and red) (Fig. 1). A well-apparent material gradient was discovered between the predominantly resilin-containing distal parts and harder basal portions of the setae. Nanoindentation experiments with the use of AFM confirmed low values of elastic modulus

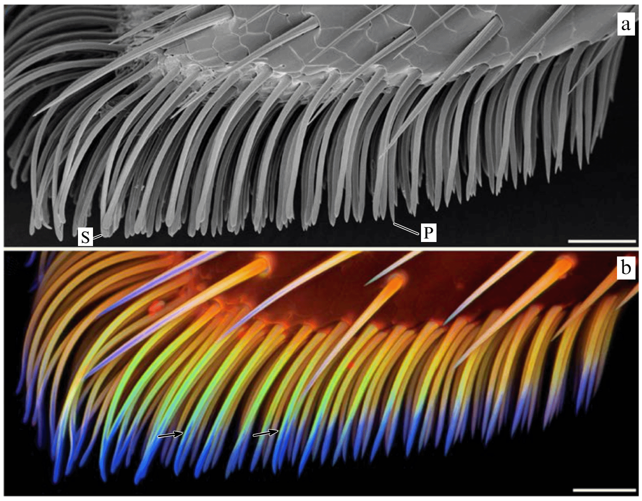


**Figure 1.** (Color online.) Morphology and composition of materials of adhesive tarsal setae. The ventral part of the second fore footpad of a female ladybird beetle (*Coccinella septempunctata*) (lateral view). (a) SEM micrograph (specimen was dried using l-propanol). (b) CLSM maximum-intensity projection showing an overlapping of the four different autoluminescences mentioned in the text. The arrows indicate the dorsoventral material gradient in exemplary setae. S — exemplary seta with spatular tips, P — exemplary seta with a pointed tip. Scale bars — 25 μm. (Take from Ref. [28].) (Photo courtesy by Nature Publishing Group. © Peisker et al., 2013.)

at setal tips [$(1.2 \pm 0.3)$ MPa] and their rise near the bases [$(2.43 \pm 1.9)$ GPa] [28].

Most biological materials are composites. Gradients of their physical properties are well known, and biological structure may give rise to unexpected new features, as was shown in earlier studies concerned with insect cuticle [33, 34], snake skin [35], human teeth [36, 37], and other biological composites. Elastic modulus gradients in smooth attachment structures on insect footpads have been reported in Ref. [38]. Interestingly, elastic modulus gradients on smooth footpads are different in locusts and grasshoppers. There are gradients on the hairy adhesive pads of ladybirds [28]. A smooth adhesive footpad consists of a soft base covered with a harder layer, in contrast to a hairy pad having a harder base and a softer tip. The existence of gradients of two different types enhances adaptability and thereby the adhesive force acting between a seta and a rough surface.

The opposite directionality of gradients can be explained by a difference in footpad architectures. Smooth footpads are formed from branching rods or cellular foams which, in combination with fluid-filled spaces between solid structures, hold the shape of the footpad. Moreover, the footpad incorporates a relatively stiff superficial layer terminating the fibers.The layer keeps the length of fiber tips at some constant value (and in species living in arid environments it protects the footpad from desiccation) [28, 39]. In hairy structures, adhesive setae are not terminated by a continuous layer and can potentially buckle and undergo clusterization [27, 40–47]. As a high degree of clusterization leads to a decrease in functional advantages from multiple contacts [23], this undesirable effect is suppressed by the presence of gradients of thickness [18] and mechanical properties [28].

To sum up, there is, as a rule, a material gradient between setal tips and bases, presumably resulting from optimization of the adhesive footpad adaptation to the rough surface over

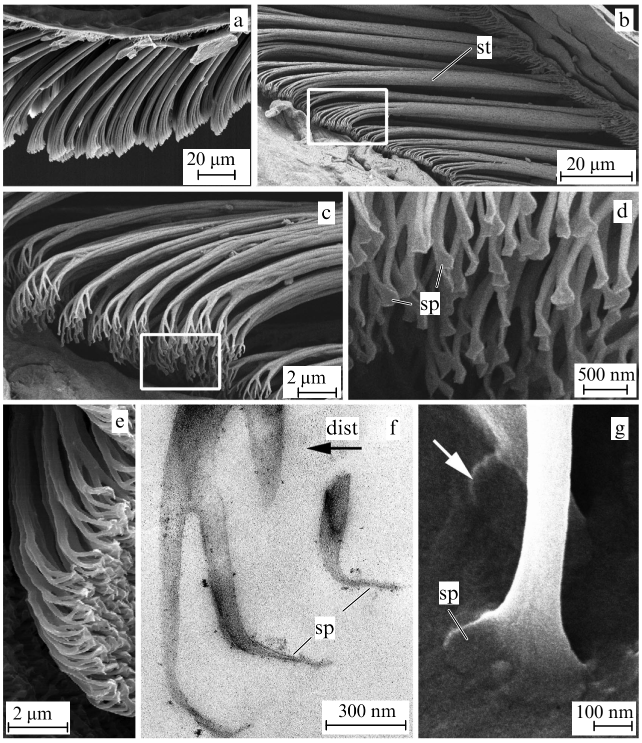


**Figure 2.** Hierarchical organization of the gecko attachment system. (a) Longitudinal cross section of the gecko foot with the lamella (thin horizontal keratinous film) covered with setae in the noncontact state. (b) Setae (st) in contact with the substrate. Setae branching into single nanofibers terminated with spatulae (sp); (c) A magnified detail shown as white rectangle in figure b; (d) A magnified detail shown as white rectangle in figure c. Orientation of spatulae in the noncontact state (e, f) and contact (g) state. Black arrow (dist) indicates distal direction of the toe in all images in this figure. White arrow points to spatula flipping from the noncontact orientation to the contact orientation.

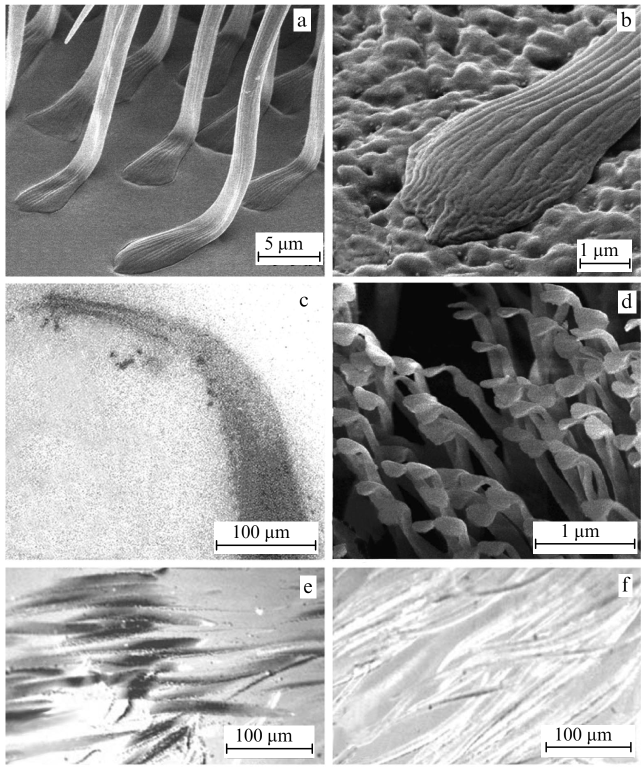


**Figure 3.** Images of terminal elements in hairy attachment pads of various animals. (a) Spatula of the beetle *Gastrophysa viridula* in contact with a flat surface (SEM image). (b) Single spatula of the same species in contact with a substrate having an average asperity dimension on the order of 300 nm. (c) Longitudinal cross section of the spatula of *Gekko gecko* (TEM image). (d) A set of spatulae of *Gekko gecko* (cryo-SEM image). (e, f) A hairy structure of the spider *Cupiennius salei* in a reflection light microscope during distal (e) and proximal (f) sliding over a glass substrate (black areas correspond to the sites of contact between spatulae and the glass surface).

the course of evolution and the simultaneous arrest of fiber clusterization. Such optimization is supposed to enhance the efficiency of the adhesive system as a whole. Although the disadvantages of purely stiff and purely soft fiber arrays are intuitively clear, it is fairly difficult to judge the advantages and disadvantages of various gradients: from the fiber base to the fiber tip or from the tip to the base, and the relationship between more rigid and less rigid areas. Numerous hypotheses treating this effect are difficult to verify in experiments with natural biological objects, which adds value to mathematical modeling of systems with such gradients.

Clusterization is a major problem facing the experimental realization of artificial adhesives motivated by the structural peculiarities behind the hairy footpads in biological species [48]. In an artificial system flexible enough to ensure excellent contact with a natural rough surface, the tiny curved hairs tend to be closer toward one another and eventually form clusters within a few attachment cycles [49, 50]. Because such clusters are usually much bigger than setae, the ability of the system to maintain good contact with a fractal surface is greatly compromised. The main problem is posed by the fact that the interaction forces responsible for cluster formation are of the same nature as the forces of attraction to the external surface [44]. Interestingly, the structure of the hairy surface on the animal footpad tends to form much fewer clusters. An important cause behind this phenomenon is the complicated spatial organization of this system. Setae extending from animal's pad lamellae form an intricate 3D structure whose complexity is much higher than all that has been hitherto created artificially along this direction. For example, the underside of the gecko's footpad is covered with so-called lamellae carrying arrays of setae 3–5 μm thick that branch out at the ends into 100–1000 separate nanofibers that, in turn, terminate in flattened, roughly 15-nm thick [11] structures (spatulae) 200 nm in length and width [1, 2, 41, 42] (Fig. 2).

Besides the fact that the division of a large adhesive contact into numerous separate contacts by itself increases the adhesive force of this fibrillar system [43–45], the effect is further strengthened by the specific spatula of each individual contact [24, 46, 47] and the fact that each seta is a constituent of a hierarchical structure at different levels (Fig. 3b, c), with each level of such multilevel architectonics being insensitive to clustering [51, 52]. An important cause of poor clusterization in a real living creature is its setal tips having a more sophisticated heterogeneous three-dimensional structure (Fig. 3) than artificial analogs [49, 50] or the structures considered in previous models [51].

Fibrillar attachment systems of insects, arachnids, and reptiles consist of setae [52–70], most of which are terminated by spatula-like rather than sharpened tips. As mentioned above, a variety of hypotheses have been proposed to explain the functional advantages of such contact geometry by an enhanced adaptability to a rough surface [32], the creation of contacts with the help of a shear force rather than normal load [1], an extension of the overall detachment line by increasing the number of spatulae [45], and contact breakage by peeling off [45, 46, 61].

It is well known that the application of a normal force may increase adhesion [63]. However, the adhesive force in hairy systems is always smaller than the applied normal force [64]. It may be insufficient to enable walking on the ceiling. Another way to improve adhesion is to apply a shear force. In this review, we present a numerical model describing the dynamics of spatula-like termini during formation of contacts with a rough surface. Specifically, it will be demonstrated for the cases of a spatula initially nonparallel to the surface that the shear increases the contact area. The force to be applied is optimal if its increase leads to contact area enlargement only until the already fixed part begins to slip. Maximum adhesion is just achieved when the pulling force is close to critical value; this observation appears to be particularly significant for biological and technical applications.

In Ref. [45], the contact between an individual element, like spatulae on the fresh footpads of various insects, and the surface was visualized by cryo-scanning electron microscopy (cryo-SEM). Some authors observed a thickness gradient extending from the base to the end of the footpad in a fly [58], gecko [59], and beetle [60] (Fig. 3b, c). The spatulae involved in the contact were aligned and oriented oppositely to the pad direction (Fig. 3a, b). Application of the shear force to the spider hairy system in a certain direction enlarged the real contact area [58] (Fig. 3e, f).

Flies, too, make shear movements in the course of establishing contacts [59]. Some authors emphasize the strong shear dependence of the measured pull-off force in the gecko attachment system and even call it 'friction adhesion' [1, 2]. The effective Young modulus for thin plates made even from relatively strong materials (e.g., keratin or arthropod cuticle) being very low, such a geometry is of fundamental importance for adhesion exhibition on rough surfaces [32] due to the low strain energy stored in the material during contact formation.

Adhesion in such systems was also shown to depend on the nature of substrate roughness [56]; the dependence is especially strong for attachment devices having predominantly spatula-like termini [21]. The importance of such contact shape for adhesion phenomenon has recently been demonstrated in experiments with artificial surfaces of analogous geometry [66–70]. The latest theoretical studies confirmed the importance of the application of a shear force to increase the pull-off strength [71]. With these observations in mind, we divided the process of numerical simulation of such systems into the following steps, which will be reproduced in the present review.

(1) First, the simplest problem of the behavior of an array of vertically fixed fibers in contact with an adhesive surface was considered, with special emphasis on determining optimal fiber elasticity.

(2) Then, these fibers of a modified model were 'allowed' to move orthogonally, which markedly enhanced their ability to adapt to surface asperities. However, the simultaneous attraction of many fiber ends to the same asperities resulted in their expected clustering.

(3) An efficient natural tool to prevent clusterization involves the use of structure gradients or (which is the same thing) the mechanical properties (stiffness) of fiber material. This option was also tested in a numerical model.

(4) One more way to avoid clusterization chosen by natural selection appears to be the nontrivial distribution of the fibers themselves in a three-dimensional space at the final level of their organization in the form of peculiar bunches suspended from a common relatively rigid root. This mode of increasing system efficiency is considered in the subsequent modification of the numerical model, with special reference to efficacious 'pulling' that causes not only the turn of spatulae during their attachment to the surface and significant enlargement of the total contact area but also a marked decrease in the clusterization effect after detachment of spatulae from the contact surface.

(5) Finally, attention was given to an important advantage provided by the structure of fiber ends with characteristic spatulae that spontaneously developed during convergent evolution in various species using adhesive attraction to rough surfaces. Also considered was the stiffness gradient along the spatula readily observable in experiment. The main problem in this context was to what extent the aforementioned 'pooling' effect promotes a better spatula adaptation to the rough surface.

These general and related concrete problems are considered in Sections 2–6 dealing with numerical simulations of such systems.

## 2. Optimal elasticity of fibers interacting with adhesive surfaces

As was mentioned in the preceding section, it is convenient to begin with constructing a simple model that concerns with the motion restricted by the vertical $z$-direction alone, which is, in turn, orthogonal to the averaged positions of two contact plates and to consider the main aspects of a numerical description of the system in this framework. In such a simple case, effective elasticity of the modelled fibers, $K_{\rm eff}$, can be regarded as an integral quantity reflecting the joint action of bending stiffness of natural setae and their stretching by molecular adhesive forces (also called van der Waals forces). The conceptual structure of such a simplified model is illustrated in Fig. 4. The solid curve reproduces a minor part of the fractal rough surface. Such a model resembles, despite its simplicity, many recently created real adhesive polymer coatings, such as the carbon filaments [10] mentioned earlier in the Introduction. These structures are much simpler than those formed in creatures by natural selection and consist of dense nanoscale setae made up of almost parallel processes assuring excellent nanoscale contact with a surface. Artificial

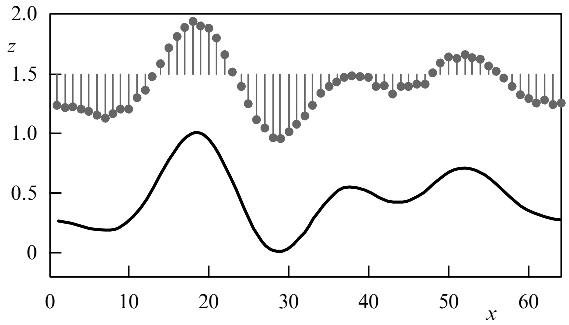


**Figure 4.** Conceptual structure of a simplified model (see the text). Solid line represents a small part of the fractal rough surface. Linear segments with dots schematically show elastic bonds.

coatings are characterized, despite their simplicity, by a very high adhesive force per unit area, $(1.6 \pm 0.5) \times 10^{-2}$ nN nm$^{-2}$, i.e., 200 times that on the gecko setal footpad. Typical strain–displacement curves obtained during a load–unload cycle suggest large adhesion hystereses up to 20-nm scale.

From the theoretical standpoint these model structures differ, of course, from natural gecko hairs, the thinnest of which ends with a tiny spatula about the size of a molecule. But, on the other hand, the simplified model allows us to confine ourselves to a description of a simple contact force taking into account only adaptation of the termini (instead of spatula) to a rough surface. Such a conceptual model developed in Ref. [14] is presented in Fig. 4. It takes into consideration both elastic interaction and the chemical potential connecting each fiber to the surface. The standard potential of this type is actually the van der Waals potential. The authors of Ref. [14] used one of the known representations of the van der Waals potential:

$$U_{\mathrm{VdW}} = -\frac{U}{12}\left[2\left(\frac{z}{z_{\mathrm{VdW}}}\right)^{-6} - \left(\frac{z}{z_{\mathrm{VdW}}}\right)^{-12}\right], \qquad (1)$$

where $U$ is the characteristic adhesion energy, and $z_{\mathrm{VdW}}$ is the potential minimum position. Each elastic hair can be strained with a respective energy

$$U_{\mathrm{elastic}} = \frac{K_{\mathrm{eff}}(z-Z)^2}{2}\,. \qquad (2)$$

Here, $Z$ denotes the equilibrium position of a hair tip. As usual, forces in equations of motion are defined by derivatives of the respective potentials:

$$F_{\mathrm{VdW}} = -\frac{\partial U_{\mathrm{VdW}}}{\partial z}\,, \qquad F_{\mathrm{elastic}} = -\frac{\partial U_{\mathrm{elastic}}}{\partial z}\,. \qquad (3)$$

For the purpose of numerical studies, it is convenient to normalize all energies, noise intensity, and spatial scales to characteristic values of physical quantities. In dimensionless units, one obtains

$$U_{\mathrm{VdW}} = -\frac{U(2r^{-6} - r^{-12})}{12}\,, \qquad U_{\mathrm{elastic}} = \frac{K(z-Z)^2}{2}\,. \qquad (4)$$

The chaotic behavior in a microscopic system is due to various causes, such as the fractal structure of the attractive surface $z = w(x)$, complicated fiber dynamics, or temperature fluctuations becoming essential on the nanoscale.

In the numerical model [14], the fractal surface can be given in the form of an $x$-coordinate-dependent data block; in accordance with the standard definition

$$w(x) = \frac{1}{2\pi}\int_{q_{\min}}^{q_{\max}} B(q)\cos(qx + \zeta)\,, \qquad (5)$$

where Fourier series coefficients have the scale-invariant form, $B(q) = c_0 q^{\alpha}$, and $\zeta(x)$ is the $\delta$-correlated random phase:

$$\langle \zeta(x)\zeta(x')\rangle = \delta(x - x')\,. \qquad (6)$$

Certainly, the real surface $w(x)$ extending from zero distances to infinity can never be truly fractal; it is so-called quasifractal including a certain limited spectrum of wave vectors $q_{\min} < q < q_{\max}$ in formula (5). Its maximum and minimum amplitudes (i.e., roughness or, in the mathematical language, standard deviation) are limited, too:

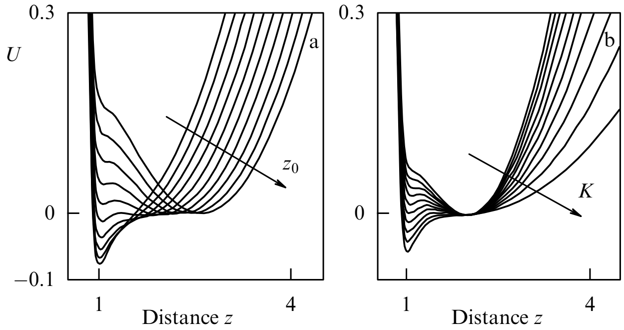


**Figure 5.** Total potential $U$ of elastic and van der Waals forces, $U = U_{\mathrm{elastic}} + U_{\mathrm{VdW}}$, calculated at a varied distance $z_0$ (a) and coefficient of elasticity $K$ (b). Arrows indicate the direction of $z_0$ and $K$ growth.

$$\Big\langle \big(w(x) - \langle w(x)\rangle\big)^2 \Big\rangle^{1/2} \leqslant A\,, \qquad (7)$$

where parameter $A$ describes the characteristic physical roughness of the surface.

In a certain region of parameters, the total potential containing adhesive and elastic components has two valleys (wells) of comparable depths. This total potential is presented in Fig. 5 in the form of families of curves calculated at different distances and elastic constants. Evidently, there are in both cases parameter regions, where the potential passes through two wells. In accordance with general principles of physical kinetics, fluctuating parameters can be expected to give rise to two alternative states of the system, with comparable energy valleys provoking dynamic jumps of the fiber ends between two (attached and detached) states. Such peculiar 'exchange of excitations' averaged over time assures attraction to the surface [14].

As a rough approximation, interhair interactions can be ignored. Then, the equilibrium is defined simply by the balance of forces: $F_{\mathrm{VdW}} = F_{\mathrm{elastic}}$. However, this seemingly trivial equation has to be solved numerically for a fractal surface. The computation procedure needs to be performed for both different distances between the surfaces and different asperities $A$. Each $A$ value gives rise to a family of relations between the attractive force and elastic constant. However, it should be taken into consideration that there are many natural surfaces with similar fractal properties on scales close to the molecular scale. Therefore, it is natural to somewhat simplify the enumeration problem as proposed in Ref. [14] by choosing an optimal close-to-unity elasticity for normalized equation (4) when roughness is, in turn, $A \approx 1$. Of course, the idealized case of $A \approx 1$ with due regard for overall normalization to parameters of van der Waals forces corresponds to practically molecular scales and almost never corresponds to reality. In fact, this means that an artificial system must combine two properties, viz. having a soft basal tissue in order for the system to preliminarily adapt to the surface on relatively large scales and comparatively stiff short asperities at the nanolevel. Such type of system modeling was undertaken in the framework of the dynamic approach. The following equations of motion were solved numerically:

$$\frac{\partial^2 z_k}{\partial t^2} = -\gamma\,\frac{\partial z_k}{\partial t} + F_{\mathrm{elastic},\,k} + F_{\mathrm{VdW},\,k} + \zeta(z_k;\,t)\,. \qquad (8)$$

Random sources $\zeta(z_k; t)$ and dissipation $\gamma\, \partial z_k/\partial t$ are included here to reproduce the influence of fluctuations (essential on such scales), which are usually a combination of thermal noise and chaotic dynamics, and can be formally described by introducing a certain effective temperature $T_{\rm eff}$ of the system:

$$\big\langle \zeta(z_{k'}; t')\, \zeta(z_k; t) \big\rangle = D\delta(z_{k'} - z_k)\, \delta(t' - t)\,, \quad D = 2k_{\rm B}\gamma T_{\rm eff}\,. \tag{9}$$

As expected for the case of parameters that are close to optimal, the dynamic chaos in a potential with two comparable minima gives rise to oscillations of the bond ends between these minima. The effective exchange interaction facilitates adaptation of the mobile surface to the rigid rough one. It resembles the effect known in the physics of friction that manifests itself as an increase in the contact area and adhesive force acting between the immobile and vibrating surfaces. The time-averaged probability $P(z)$ of discovering the end of a fiber at arbitrary $z$, computed for the optimal relationship between two types of interactions, is shown in Fig. 6.

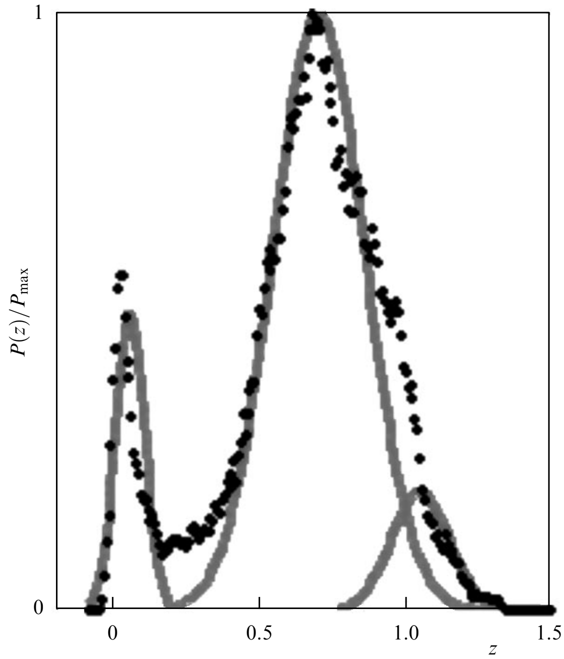


**Figure 6.** Time-averaged histogram of probability of finding the end of a fiber in position $z$, normalized to its maximum value, $P(z)/P_{\rm max}(z)$. Gray solid curves denote numerical expansion of the histogram into three main states (near each of the surfaces and intermediate).

It is worthwhile to note without going into detail that the numerical experiment was carried out for various surface roughnesses (with different mean distances between contact surfaces) and for three different relations between elastic constants: $K < K_{\rm opt}$, $K \approx K_{\rm opt}$, and $K > K_{\rm opt}$. The results of modeling are presented in Figs 7a, b, and c, respectively. Each vertical cross section shown in grayscale corresponds to a concrete realization of the $P(z)/P_{\rm max}(z)$ histogram. The darker the color, the greater the probability $P(z)$.

It follows from Fig. 7 that, since the elastic constant is too large, all bonds are mainly attracted to the upper plate. They do not fit properly to the rough surface, and the total attractive force is too small. In the opposite limit, all fibers fit the stiff surface 'ideally'. But the corresponding 'springs' are too weak in this case to detach them and bring them back into the initial positions if necessary. Very strong extension and huge hysteresis are needed to pull this sticky system as a whole off the adhesive surface. Of course, such a mechanism is highly inefficient from both biological and technical standpoints. These data give evidence that an optimal hair elasticity actually exists in such a system. Moreover, as it turned out the corresponding fibers must be stiff enough, despite intuitive expectations.

It is worthwhile to note that a compromise between fiber stiffness and good adaptation to the surface is also principally possible due to a certain reserve of attraction, because even already created systems are to a certain extent 're-armed' and capable, theoretically, of maintaining a stronger attraction than is necessary for practical applications. An additional adaptation can be reached by virtue of hair motion (rotation, bending) in the horizontal directions, which we have thus far disregarded. In this case, the hairs are able to find asperities on the stiff rough surface located relatively close to but not immediately above them. This option is discussed in Section 3.

## 3. Elastic tissue with attached fibers interacting with an adhesive surface

In Section 2, we described the procedure of numerical modeling of an artificial structure composed of fibers in contact with a rough surface owing to van der Waals forces. The objective of simulations was to find an optimal relation between the parameters in the case of strong enough limitations, one of them being the solution of the force balance equations for a $1+1$-dimensional system with a

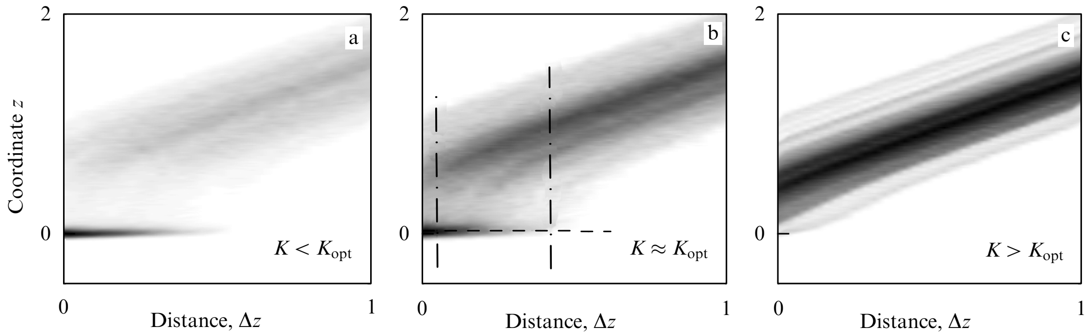


**Figure 7.** Grayscale maps for density histograms and different relations between elastic constants: (a) $K < K_{\rm opt}$, (b) $K \approx K_{\rm opt}$, and (c) $K > K_{\rm opt}$. Dash-dotted lines in figure b distinguish the elasticity interval in which the fiber ends are distributed mainly in the middle between the surfaces.

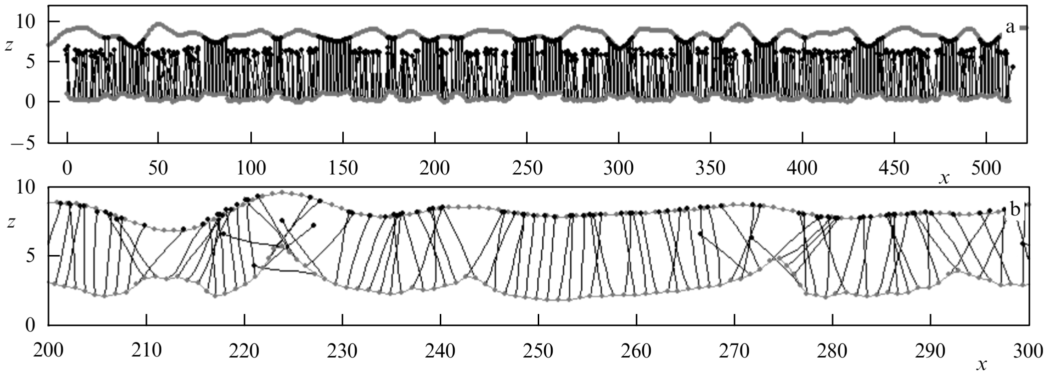


**Figure 8.** Conceptual structure of the generalized model (see the text). (a) An early stage of the contact with a variety of disconnected bonds. The lower and upper bold lines represent parts of the rough surface and flexible tissue, respectively. The lines with black dots show instantaneous positions of elastic hairs. (b) A closer view of the same system at a later stage of the process when the fibers are distorted and inclined in search of close-to-ideal conditions for contact with the surface.

hair motion allowed only in the vertical direction. Such a model, despite its mathematical simplicity and convenience, needs to be further elaborated, in the first place to include consideration of movements in the direction orthogonal to the vertical one. There are numerous experimental data suggesting the significance of such movements, besides purely theoretical predictions. Specifically, slippage or vibration in the direction orthogonal to the vertical one can transfer the energy of macroscopic displacements deep down to microscopic scales to improve surface adaptation and increase contact area [11, 13, 15, 16]. In what follows, the model described in the preceding section will be extended to take account of this additional degree of freedom. We shall also consider how the attraction intensity and the film attachment and detachment scenarios at all depend on various initial distances, surface heterogeneity, and tilt angles. The conceptual structure of the generalized model is illustrated in Fig. 8. The stiff adhesive surface is shown by the bold line, while thin lines ending with dots denote fibers. Figure 8a depicts the early stage of the process during which most bonds are still broken. Figure 8b represents a magnified part of the same system at the later stage when many fibers are inclined and bent to facilitate contact. Generally speaking, the fibers cannot acquire an absolutely optimal configuration and therefore take a certain intermediate position determined by the 'frozen-in kinetics' of the search for such a position. The resulting configuration can be found only numerically by solving the respective equations of motion.

On the whole, the equations remain the same as in Section 2, but the one-dimensional van der Waals potential is substituted by the two-dimensional one:

$$U_{\mathrm{VdW}} = -\frac{U}{12}\left[2\left(\frac{|\mathbf{r}|}{r_{\mathrm{VdW}}}\right)^{-6} - \left(\frac{|\mathbf{r}|}{r_{\mathrm{VdW}}}\right)^{-12}\right], \tag{10}$$

where $U$ is the characteristic adhesion energy amplitude (as before), $\mathbf{r} = \{x, z\}$ is the two-dimensional vector, and $r_{\mathrm{VdW}}$ is the position of the potential maximum in two-dimensional space. However, more intricate changes are needed in the elastic component of interaction. First, to be able to bend, elastic hairs must be composed of a large enough number of separate segments with the ends having coordinates $\{r_i, r_j\}$, $j = 1, 2, \ldots, n_{\max}$. To shorten calculations, it can be assumed by way of compromise that only the end of the last segment interacts with the surface via the van der Waals potential, which means that the term $U_{\mathrm{VdW}} = U_{\mathrm{VdW}}^{n_{\max}}$ in the energy acts only at $j = n_{\max}$. In the zero approximation, it is possible, as before, to sacrifice the interaction between separate fibers. Each elastic segment can be extended (contracted) with the elastic energy

$$U_{\mathrm{elastic}}^{ij} = \frac{K_{\mathrm{eff}}(r_i - r_j)^2}{2}\,. \tag{11}$$

The essentially new part in the energy of the generalized model compared with that described in Section 2 is related to the possibility of fiber bending. Mathematically, such energy must be constructed so as to prevent mutual deflections of the vectors directed along each of the two nearest segments:

$$U_{\mathrm{bending}} = K_{\mathrm{bending}}\left[1 - \frac{(r_j - r_{j+1})(r_{j-1} - r_j)}{|r_j - r_{j+1}|\,|r_{j-1} - r_j|}\right]. \tag{12}$$

The forces corresponding to these components of the model are defined now by derivatives of all contributions to the energy along the two orthogonal directions:

$$F_{\mathrm{VdW}}^{z} = -\frac{\partial U_{\mathrm{VdW}}}{\partial z}\,, \qquad F_{\mathrm{VdW}}^{x} = -\frac{\partial U_{\mathrm{VdW}}}{\partial x}\,,$$
$$F_{\mathrm{elastic}}^{z,ij} = -\frac{\partial U_{\mathrm{elastic}}^{ij}}{\partial z}\,, \qquad F_{\mathrm{elastic}}^{x,ij} = -\frac{\partial U_{\mathrm{elastic}}^{ij}}{\partial x}\,,$$
$$F_{\mathrm{bending}}^{z,j} = -\frac{\partial U_{\mathrm{bending}}^{j}}{\partial z}\,, \qquad F_{\mathrm{bending}}^{x,j} = -\frac{\partial U_{\mathrm{bending}}^{j}}{\partial x}\,.$$

Let us introduce dimensionless units, as in Section 2, with the help of normalization to basic parameters of the system $F_{\mathrm{VdW}}, \zeta_{\mathrm{VdW}} < 10$, $S = 0.1K$. In these units, one obtains

$$U_{\mathrm{VdW}} = -\frac{U}{12}(2r^{-6} - r^{-12})\,, \qquad U_{\mathrm{elastic}}^{ij} = \frac{K(r_i - r_j)^2}{2}\,,$$
$$U_{\mathrm{bending}}^{j} = S\left[1 - \frac{(r_j - r_{j+1})(r_{j-1} - r_j)}{|r_j - r_{j+1}|\,|r_{j-1} - r_j|}\right]. \tag{13}$$

The fractal surface is given in the same way as in Eqns (5)–(7):

$$z = w(x) = \frac{1}{2\pi}\int_{q_{\min}}^{q_{\max}} B(q)\cos(qx + \zeta)\,,$$

with similarly truncated wave vectors: $q_{\min} < q < q_{\max}$. All the distances are measured in terms of a fixed interval between the two nearest fibers, chosen for definitiveness to be

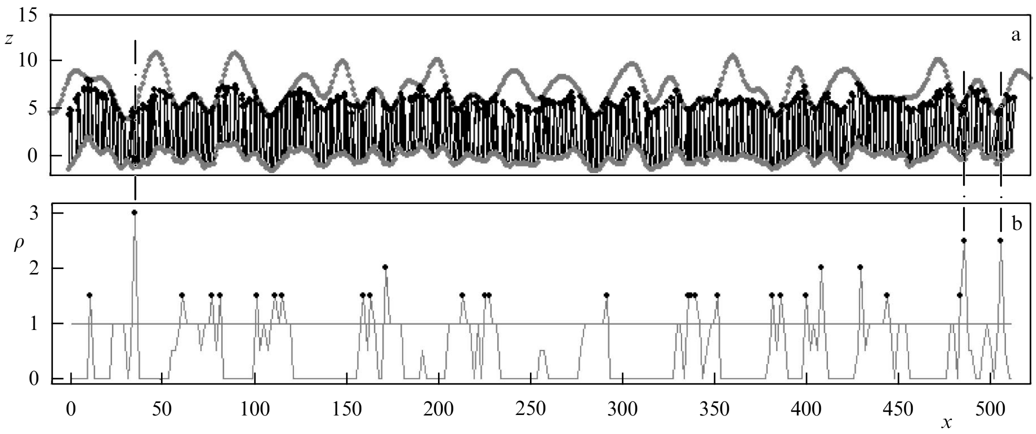


**Figure 9.** Comparison of instantaneous spatial positions of fiber attachments to a surface (a) with the extrema of nonuniformly distributed density, and (b) normalized to the mean fiber density in the system shown by the horizontal straight line at the unit level. Some regions with a high density of the fiber spatial localization are marked by vertical dash-dotted lines passing through figures a and b.

$\Delta x_k = \text{const} \equiv 1$ nm, while the roughness amplitude varies up to $A_{\max} = 10\Delta x_k$. The elastic constant $K = 1$ is chosen in the same units of adhesion forces and distances; accordingly, the stiffness is $S_{\max} = 10K$. The last assumption needed to write down equations of motion refers to elastic film strains. Let us assume that the root segment of each fiber is rigidly attached to the film. This means that the coordinates of tissue segments coincide with the positions of the first tissue elements: $\{x_k^{j=1}, z_k^{j=1}\}$. Moreover, the model film is assumed to have inherent elasticity in the vertical direction:

$$U^1_{\text{elastic}} = \frac{K_1^z}{2}\left[(z_k^1 - z_{k+1}^1)^2 + (z_k^1 - z_{k-1}^1)^2\right],$$

while the distance between its segments in the horizontal direction is given to unambiguously define the fiber array: $\Delta x_k = \text{const} \equiv 1$. To maintain a force balance in the vertical direction $z$, the film is supported by a certain external force $F^z_{\text{external}}$ which results in the appearance of two boundary conditions for coordinates $\{z_k^{j=1}\}$:

$$F^{z,1}_{\text{elastic}} = -\frac{\partial U^1_{\text{elastic}}}{\partial z}\,, \qquad F_k^{z,1} = F^z_{\text{external}}\,. \tag{14}$$

The entire system of dynamic equations under these conditions can be represented in the form

$$\begin{aligned}
\frac{\partial^2 z_k^j}{\partial t^2} &= -\gamma\,\frac{\partial z_k^j}{\partial t} + F^{z,\,ji}_{\text{elastic},\,k} + F^{z,\,j}_{\text{bending},\,k} + F^{z,\,j=n_{\max}}_{\text{VdW},\,k} \\
&\quad + \delta_{j1}\left(F^{z,1}_{\text{elastic},\,k} + F^z_{\text{external}}\right) + \zeta(x_k^j, z_k^j; t)\,, \\
\frac{\partial^2 x_k^j}{\partial t^2} &= -\gamma\,\frac{\partial x_k^j}{\partial t} + F^{x,\,ji}_{\text{elastic},\,k} + F^{x,\,j}_{\text{bending},\,k} + F^{x,\,j=n_{\max}}_{\text{VdW},\,k} + \zeta(x_k^j, z_k^j; t)\,.
\end{aligned} \tag{15}$$

Here, $\delta_{j1}$ is the Kronecker symbol. The random source $\zeta(z_j; t)$ and terms $\partial z_j/\partial t$ included in the system are now modified, too, taking into account the two-dimensionality and multiparticle nature of the problem:

$$\begin{aligned}
&\left\langle \zeta(x_k^j, z_k^j; t)\,\zeta(x_{k'}^{j'}, z_{k'}^{j'}; t')\right\rangle = D\delta(x_{k'}^{j'} - x_k^j)\delta(z_{k'}^{j'} - z_k^j)\delta(t' - t)\,, \\
&D = 2k_{\mathrm{B}}\gamma T_{\text{eff}}\,.
\end{aligned} \tag{16}$$

The totality of numerical experiments with system (15) was organized as follows. A new realization of the rough surface was numerically generated every time, and the film being bent was placed at a priming distance $z_0$. The film was initially taken to be flat (given by a straight line in the two-dimensional model) and the fibers were arranged orthogonally to the film in the form of a regular sequence. At the beginning, the system was allowed to move naturally in accordance with equations of motion and boundary conditions (15), (16) and thereby gradually reach an equilibrium (generally speaking, different for each realization). The time taken to reach such an equilibrium can be formally estimated using the relaxation constant: $t_{\max} \propto \gamma^{-1}$. However, as the proportionality coefficient is unknown, the *a posteriori* estimation appears to be more reliable; in other words, it should be revived after all quantities being calculated begin to exhibit the stationary asymptotic behavior. For the problem under consideration, such a process usually takes time $t_{\max} \approx 200\gamma^{-1}$.

There is no need to reproduce here all steps and results of this time-consuming process. Suffice it to note that at its intermediate stage the fiber tips as a rule most intensely move along the surface in the horizontal direction. It is the ability of the fiber tips to move horizontally that distinguishes this variant of the model from the one considered in Section 2 [14, 15]. The transverse motion just accounts for the highly nonuniform distribution of bristles. It can be argued that such a *rearrangement in the horizontal direction compensates for the fractal structure in the direction of the z-axis*.

Figure 9a illustrates the typical fiber redistribution at the intermediate stage of system evolution during which a nonuniform fiber density gradually forms, as shown in Fig. 9b for comparison, $\rho_0 = N_{\text{fibers}}/L_{\text{tissue}}$. For convenience of comparing with the real spatial distribution, the regions of especially high density are marked in Fig. 9a by vertical dash-dotted straight lines.

Naturally, the mechanical properties of the system depend on fiber stiffness, film roughness and elasticity. Therefore, the numerical experiments were conducted in a wide range of all these parameters. They revealed, despite minor concrete distinctions, one common principal feature: *fiber distortion in the horizontal direction compensates for the fractal structure in the vertical direction* at various roughness amplitudes up to rather large ones. Admittedly, strong spatial distortions markedly affect, however, film peeling off the surface, because a variety of fibers attached to the same surface asperities detach from them almost simultaneously (avalanche-like detachment), making one of the most important

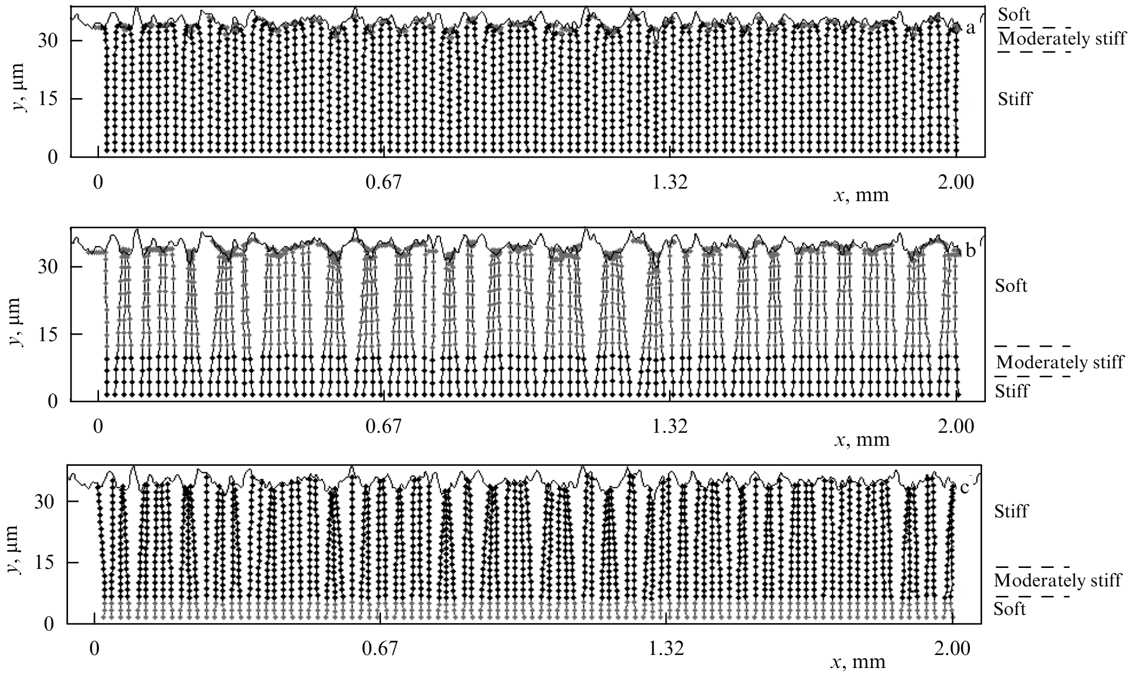


**Figure 10.** Typical configurations of the filamentary adhesive structure attached to the stiff support (below) with the random fractal surface (above). Three types of fibers: (1) long stiff ones with short elastic ends, (2) long elastic ones connected to the base by short stiff roots, and (3) relatively stiff ones with short elastic segments connected to the base are shown in the panels (a), (b), and (c), respectively. Different stiffnesses of segments are conditionally shown by dots with different colors. Stiff, medium, and soft segments are marked by black, dark gray, and light color dots, respectively.

approximations of the model (*approximation of noninteracting fiber ends*) *excessively artificial*. As a matter of fact, the forces of interaction between fiber ends must be of the same nature as their adhesion to the surface, i.e., comparable with it. In this case, the fibers arranged in bundles near surface asperities can remain joined together even after detachment from the surface. This effect, its consequences, and possible preventive measures are discussed in Section 4.

## 4. Fibrillar adhesion with no clusterization: functional significance of material gradient in the insect adhesive setae

This section is designed to consider the following issues: (1) does a material with a composition gradient, as opposed to one without such a gradient, contribute to proper contact formation?, and (2) does the material gradient reduce the tendency toward clustering?

To analyze the influence of setal gradient properties, we constructed a simple but still realistic model taking into consideration interfiber interactions and only partly including, for operation speed, elements of the models described in Sections 2, 3. An array of initially parallel fibers is attached to a rigid base. The gradient of properties is apparent as continuous variation of fiber elasticity (of corresponding force $F_{\mathrm{elastic}}$) along their length, from very soft to much harder (practically rigid). Longitudinal ($\mathbf{F}_{jk}^{\parallel}$) and transverse ($\mathbf{F}_{j}^{\perp}$) setal stiffnesses are reproduced through interactions between discrete segments of the fibers:

$$\mathbf{F}_{jk}^{\parallel} = K^{\parallel}(\mathbf{r}_j - \mathbf{r}_k)\left[1 - \frac{(\mathbf{r}_j - \mathbf{r}_k)^2}{\mathrm{d}r^2}\right],$$
$$\mathbf{F}_{j}^{\perp} = K^{\perp}(2\mathbf{r}_j - \mathbf{r}_{j+1} - \mathbf{r}_{j-1}).$$

Here, we confine ourselves to a two-dimensional model in which vectors $\mathbf{r}_j = \{x_j, y_j\}$ are given by the coordinates of the beginning of the segment numbered $j$, $k = j \pm 1$. Longitudinal force $\mathbf{F}_{jk}^{\parallel}$ is defined by the potential with two valleys that tends to maintain a constant distance between points $\mathbf{r}_j$ and $\mathbf{r}_{j\pm1}$, close to the equilibrium length $\mathrm{d}r$ of a segment. Transverse force $\mathbf{F}_{j}^{\perp}$ holds $\mathbf{r}_j$ close to the mean distance between a pair of neighbors $(\mathbf{r}_{j+1} + \mathbf{r}_{j-1})/2$ and keeps a constant angle of 180° with the neighboring segments.

Bearing in mind forces of different natures used by animals and discussed in Sections 2, 3, we assume that a surface attracts fiber ends by the totality of capillary and molecular forces. To increase computation speed in the model of interest, the attraction is specified in the simplest mode, namely, by the gradient of the Morse potential $U_{\mathrm{VdW}}(r) = U_0(1 - \exp(-r/r_0))^2$ with a certain physically reasonable amplitude $U_0 = 10$ nN nm and the minimum located at the distance $r_0 = 0.01$ μm from the surface. As above, the stiff fractal surface [24] has a given spectrum $C(q) = 1/q^{\beta}$, $\beta \approx 0.9$ and a roughness amplitude comparable to the distance to the potential minimum: $A = r_0$. The terminal portions of each fiber interact with one another. Because this interaction is of the same nature as the attraction to the surface, it can be described for simplicity by the same potential $U_{\mathrm{interact}}(r_{jk}) = U_0[1 - \exp(-r_{jk}/r_0)]^2$ with comparable characteristic parameters $U_0$, $r_0$. To increase computation speed, we may confine ourselves to attractive interaction between the nearest neighbors: $r_{jk} = |r_j - r_{j\pm1}|$. On these scales, the system can be regarded as overdamped, with the equation of motion including only the first time derivative $\partial r/\partial t = F$. The total force in this equation accumulates all the above-described contributions: $F = F_{\mathrm{elastic}} + F_{\mathrm{VdW}} + F_{\mathrm{interact}}$.

The model is schematically represented in Fig. 10. The stiff surface is marked by bold curves. To elucidate the

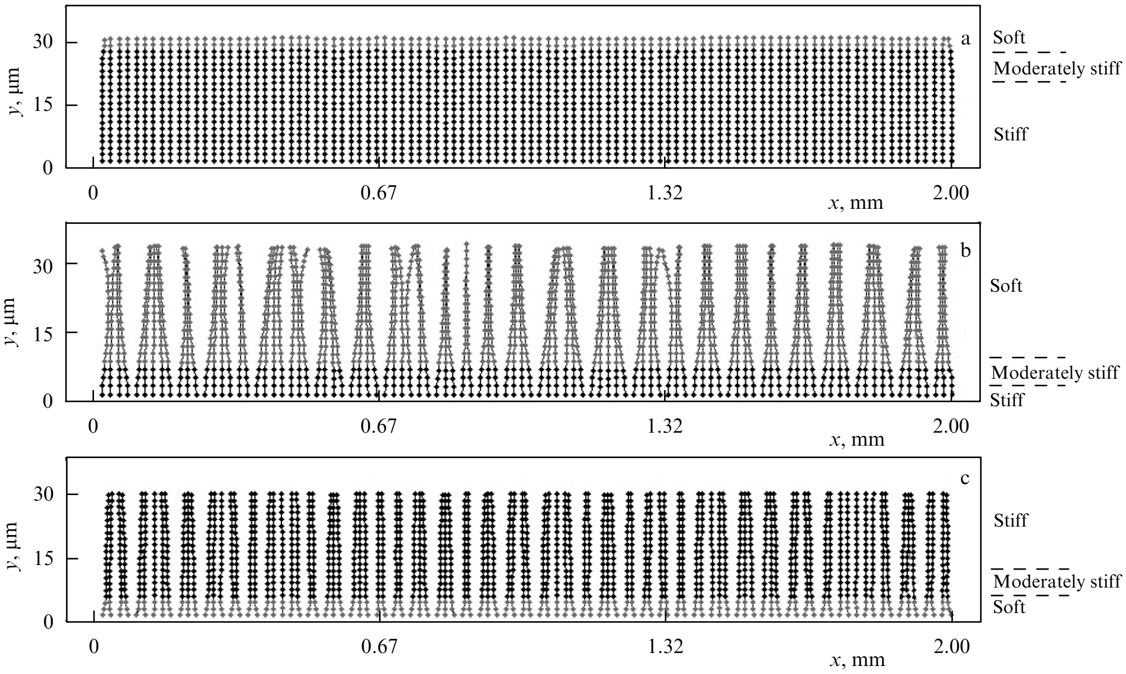


**Figure 11.** Same system, as presented in Fig. 10, shown after fiber detachment from the fractal surface and sufficiently long relaxation to the steady state. The difference between a highly clustered system having either long elastic fibers (b) or long stiff fibers with soft bases (c) and a system with short soft ends (a) which practically returns to its original configuration is clearly seen.

functional role of the material property gradient [25], three types of fibers were considered: (a) long stiff ones with short elastic ends, (b) long elastic ones connected to the basal plate by short stiff roots, and (c) relatively stiff ones with short elastic segments attached to the basal plate. These types are illustrated in Figs 10a, b, and c.

In all cases, the stiffness of the fibers continuously varies along the vertical coordinate and is universally described by the smoothed step-function $\Theta(y) = 1/[1 + \exp(-(y - y_0)/\Delta)]$ with regulated position of bend $y_0$ and step width $\Delta$. The function $\Theta$ tends to unity when $y \ll y_0$, and gradually goes to zero in the opposite limit, allowing modeling all the aforementioned cases with a common approach. To illustrate the different stiffnesses of fiber segments shown in Fig. 10, the stiffness was formally divided into three groups: (1) close to the maximum, (2) less than half of the maximum (a region around $y_0$ with width $\Delta$), and (3) less than 0.1 of the maximum. These parts are conditionally shown in the plots by different colors. Stiff, medium, and soft segments are marked by black, dark gray, and light dots, respectively.

The numerical procedure was organized as follows. The computer procedure brings an array of originally unperturbed (equidistant and parallel) fibers attached to the horizontal hard base into contact with the numerically generated rigid fractal surface. The fibers undergo distortions as they interact with the fractal surface and among themselves. Due to surface heterogeneity, many of them are attracted to the same individual asperities of the surface and thereby become gathered into distinctive bundles. For numerical control, it is convenient to record not only time-dependent distortions of the fibers but also variations of the interfiber attractive forces. When the system reaches a stationary configuration, the process of contact formation stops. Then, the fractal surface can be formally 'removed' to observe relaxation of the system to some new stationary state. This procedure allows us to examine whether the system returns to the initial state and how much time the return, if any, may take. After elimination of the fractal surface, the mutual attraction of the fibers collected into bundles competes only with the elastic forces inside the fibers, and the further behavior of the system wholly depends on the magnitude of these forces and their spatial distribution. The distribution turns out to be different in the above three cases. The results of their simulation are qualitatively given in Fig. 11 showing the final configurations of fiber arrays in reaching the stationary state after removal of the fractal surface. The figure demonstrates the very apparent distinction between a highly clustered system having either long elastic (Fig. 11b) or long stiff (Fig. 11c) fibers with soft bases and a system having long stiff fibers with short elastic ends. Only the latter system practically returns to the original configuration.

Thus, a system returns to the initial state if fibers have flexible enough ends and stiff shafts almost undeformable along the remaining length. Such a structure can theoretically result in strong deformation of the fiber ends and an insufficiently high total adhesive force. To verify this assumption, it is necessary to compare adhesive forces in the above-distinguished three cases: a, b, and c (see Fig. 11). These forces were accumulated throughout the entire system during the total attachment time. The maximum forces in cases (a) and (b) are comparable. Moreover, the potential barrier, i.e., the difference between force maximum in the beginning and its minimum after the system perfectly adapts itself to the surface, is even higher in case (a). Qualitatively, this effect occurs due to the fact that flexible fiber ends are too long in case (b), whereas in case (c) (long almost rigid rods rotating about flexible bases) a good enough adaptation to the surface is practically unattainable. This accounts for the significantly smaller maximum of the attraction force in case (c) than in cases (a) and (b).

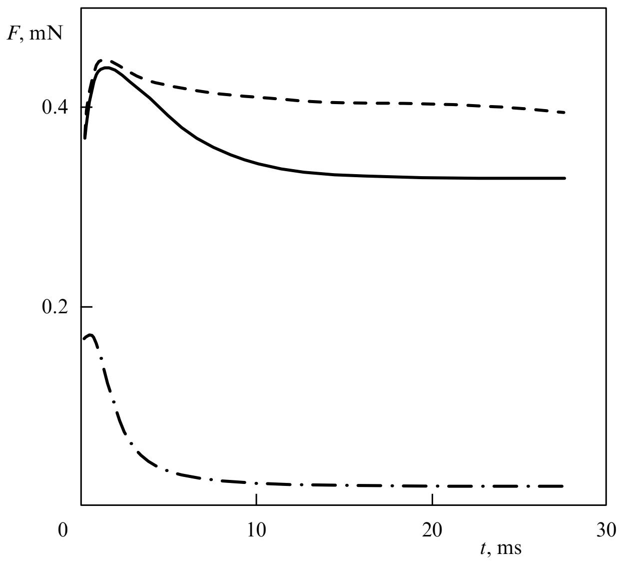


**Figure 12.** Time-dependent total vertical forces generated during the entire period of attachment to the fractal surface of an initially unperturbed system, integrated over the entire length. Solid, dashed, and dash-dotted curves correspond to cases a, b, and c, respectively, in Figs 10 and 11.

Time-dependent information about fiber strain is convenient to accumulate by introducing arrays of distances $\{\mathrm{d}x_j\}$ between contact ends of the nearest neighbors: $\mathrm{d}x_j = x_{j+1} - x_j$, $j = 1, 2, \ldots, N_x$. The temporal evolution of each array during an entire attachment–detachment cycle for all three cases (a–c) is illustrated in Fig. 12. Each line in the figure corresponds to one concrete time-dependent distance for a pair of nearest neighbors: $\mathrm{d}x_j = x_{j+1} - x_j$. All the distances are normalized to the initial distance in an unperturbed homogeneous array, so that $\mathrm{d}x_j = 1$ at $t = 0$.

The evolution of the process is quite apparent from these diagrams. When many fibers are simultaneously attracted to an individual asperity of the surface and form clusters, the distance between their ends virtually vanishes: $\mathrm{d}x_j = x_{j+1} - x_j \to 0$. At the same time, the distance between fibers in different clusters in general increases. It must correlate with the characteristic distance between surface asperities, but actually remains random due to the random distribution of the asperities (with the characteristic spectral distribution) over the fractal surface. An ultimately 'frozen' configuration is a result of a compromise between fiber flexibility, the force of fiber attraction to a surface, and the fiber mutual attractive force.

After removal of the surface, the fiber array relaxes to a new stationary configuration depending only on a compromise between elasticity and the mutual attraction of the fibers. In the large time limit, the fiber distribution does not directly depend on the surface structure and is determined mostly by material stiffness and gradients. However, the fiber distribution can keep a memory of the asperity distribution over the surface, specifying the concrete realization of clusters. At this stage, depicted in Fig. 13, the time-dependent process is consistent with intuitive expectations. Specifically, the distance array returns to its initial distribution only when comparatively stiff almost everywhere fibers have short flexible tips. Although Fig. 13 presents a comprehensive pattern of the evolution of time-dependent arrays, the overlap of many individual trajectories makes it difficult to visually estimate the frequency with which concrete distances encounter one another in the system. It is convenient to treat these arrays based on distribution histograms $P = P(\mathrm{d}x)$ of distances $\mathrm{d}x_j = x_{j+1} - x_j$ for each time instant. This information is represented in Fig. 14.

The numerical experiment described in this section has demonstrated that fibers with a gradient structure and high stiffness over almost the entire length with relatively short soft ends have an advantage over those with other combinations of parameters. Such gradients have recently been described in beetles [28]. However, it can be supposed now that analogous gradients must have developed in various groups of arthropods over the course of convergent evolution.

## 5. Spatial model of gecko footpad hairy structure: functional significance of highly specialized nonuniform geometry

The data presented in Sections 2–4 provide a basis for constructing a three-dimensional model with a complicated spatial geometry and nonuniform distribution of branch properties in order to clarify the advantages of such a structure over that exhibiting a flat spatial geometry.

The discrete numerical model is organized as follows. Imagine a rigid rod fiber which is initially directed at some angle $\varphi_{t=0} = \varphi_0$ to the contact surface and is placed at some

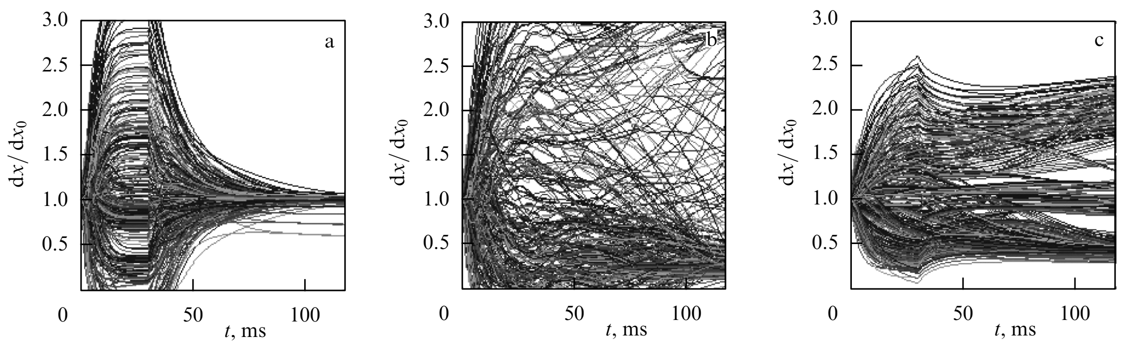


**Figure 13.** Temporal evolution of arrays $\{\mathrm{d}x_j\}$ of distances, $j = 1, 2, \ldots, N_x$, between the ends of nearest neighbors $\mathrm{d}x_j = x_{j+1} - x_j$ during individual fiber attachment–detachment cycles for the three cases (a–c) shown in Figs 10–12. All the distances are normalized to the initial period of the original unperturbed system: $\mathrm{d}x_j = \mathrm{d}x_0$ at $t = 0$. Each line in the plots corresponds to the distance in one pair of the neighbors: $\mathrm{d}x_j = x_{j+1} - x_j$. In the attached state, each of the attachment system by itself tends to a configuration which represents a certain compromise among fiber stiffness, adhesion to the array of surface asperities, and mutual attraction of the fibers. After detachment, the system relaxes to the asymptotic configuration corresponding to a compromise between the fiber stiffness and mutual attraction of the produced clusters only.

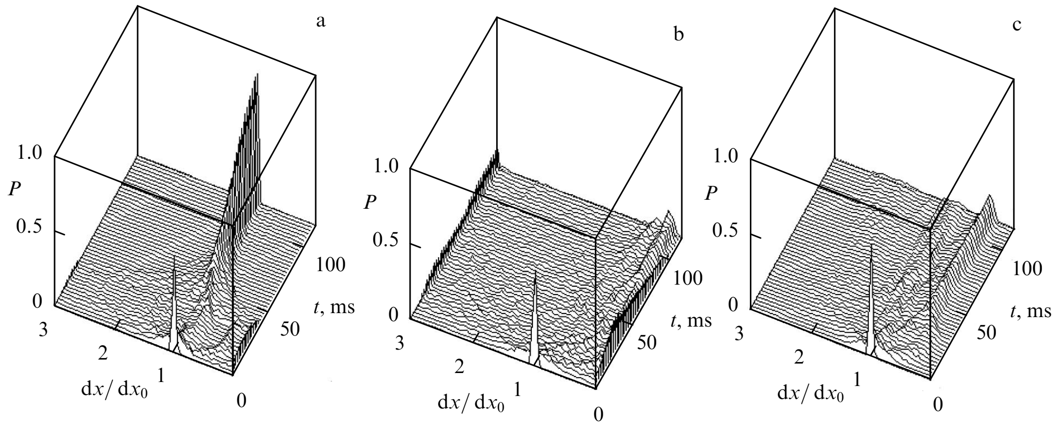


**Figure 14.** Statistical analysis of the trajectories presented in Fig. 11. The sequences of the histograms show time evolution of the probability of finding a particular value of the distance between the nearest neighbor fibers $dx_j = x_{j+1} - x_j$ in each concrete interval. Cases (a)–(c) are the same as in Figs 10–13. Starting from an unperturbed configuration (single peak around $dx_j = dx_0 = 1$), all the systems evolve in the contact to relatively smoothed distributions with a very apparent maximum at $dx \approx 0$, which corresponds to clusterization. After detachment from the surface, only the distribution presented in figure (a) returns to the state with the solitary peak $P(dx)$ around $dx_j = dx_0 = 1$ that almost ideally coincides with the initial one.

fixed distance from it. A set of thinner elastic fibers is attached to the rod. The conceptual structure of the model is shown in Fig. 15. For definiteness, the number of elastic fibers is put to 10 ($N_x = 10$), and each fiber is constructed of 50 elastic segments ($N_y = 50$), each having the length $dR = 0.04$ μm, to correspond to the total length of each fiber according to the measurements with scanning electron microscopy (SEM) images (see Fig. 13). The fibers are provided with longitudinal ($K^{\parallel}$) and transverse ($K^{\perp}$) stiffnesses. (For certainty and for simplicity of the model, it is assumed that $K^{\parallel} = K^{\perp}$.) A strain of fibers produces elastic forces proportional to their stiffness. The longitudinal force $\mathbf{F}^{\parallel}_{jk}$ is described by a double-well potential constructed to keep a distance between the nodes $\mathbf{R}_j$ and $\mathbf{R}_{j\pm1}$ close to the equilibrium length $dR$ of the segment: $\mathbf{F}^{\parallel}_{jk} = = K^{\parallel}(\mathbf{R}_j - \mathbf{R}_k)\{1 - [(\mathbf{R}_j - \mathbf{R}_k)/dR]^2\}$, where $\mathbf{R}_j$ is a position of the vector in the middle of segment $j$, $k = j \pm 1$. This form of the longitudinal force was chosen so as to be linear at small deflections, but increase nonlinearly at large deflections, and be able to suppress them. The presence of these two terms (linear and nonlinear) causes a minimum of the effective potential at equilibrium length $dR$. The second force $\mathbf{F}^{\perp}_j$ is directly proportional to the lateral deflections and tends to keep $\mathbf{R}_j$ close to the position in the middle between its nearest neighbors: $\mathbf{F}^{\perp}_j = K^{\perp}(2\mathbf{R}_j - \mathbf{R}_{j+1} - \mathbf{R}_{j-1})$.

The initial configuration of the fibers was constructed in a manner to mimic as much as possible the form of such a structure in a real animal, shown in Figs 2, 3. Each of the fibers is elastically attached to the unit rigid root rod (bold straight line in Fig. 15). The fibers have different lengths and orientations. As a result, their ends are shifted one from another in all three dimensions: both parallel to the line of the common base and in two orthogonal directions. To mimic better the natural structure, individual initial positions of every single segment were generated numerically. The resulting configuration is shown in the conceptual image (see Fig. 15). It reproduces, among other things, the correct original orientation of the terminal parts (spatulae) of the fibers that are turned backward to the root rod and their orientation in the attached state. According to the main hypothesis, all these components of the structure are essential for its functional efficiency.

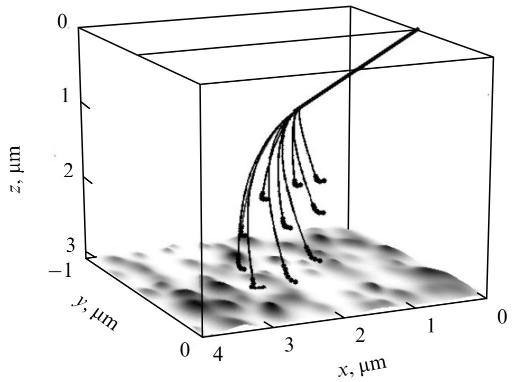


**Figure 15.** Conceptual three-dimensional structure of the model system. The bold straight line corresponds to the root segment. Thin lines reproduce filamentous nanofibers terminated by spatulae. Black dots at the ends of the curved lines mark extremely flexible spatula regions. Fractal surface $z$ generated by the two-dimensional generalization of the one-dimensional procedure is shown in grayscale above the $xy$ plane. The $z$-coordinate of the whole plot is flipped upside down in order not to shadow the fibers by the fractal surface from above.

Importantly, an additional degree of freedom in a real system comes from the rotation of the relatively rigid root rod. To reproduce it in the model, rotational stiffness $B$ is introduced, which dynamically tends to keep the root rod angle $\varphi$ close to a certain priming angle $\varphi_0$ without interfering with its rotation. In the first approximation, the appropriate rotational force acting on the root rod is linearly proportional to the difference $\varphi_0 - \varphi$: $f^{\varphi} = B(\varphi_0 - \varphi)$. For $B$ greater than 0, the force tends to restore the angle $\varphi$ to its equilibrium value $\varphi_0$. As a result, the whole system rotates under the combined action of this and remaining forces with respect to its initial position, when the fibers are either attracted to it or forced to move away.

The surface in three-dimensional space is generated by the real part of function

$$Z(x, y) = A \iint dq_x \, dq_y \, B(q) \exp\left(iq_x x + iq_y y + \zeta(x, y)\right)$$

with power-like spectral density $B(q) = 1/q^\beta$, $\beta \approx 0.9$. As before, the attraction to the surface is caused by the intermolecular force given by potential $U_{\mathrm{VdW}}(r_j) = U_0[1 - \exp(-r_j/r_0)]^2$, where $r_j$ is the distance between the end of each $j$th segment of a fiber and the surface $Z(x, y)$, $U = 10$ nN nm, $r_0 = 0.01$ μm, and $A = r_0$. Flexible and thin parts of every fiber interact with corresponding segments of other fibers in the array. This interaction has the same origin as their attraction to the stiff substrate:

$$U_{\mathrm{interact}}(r) = U_0\left[1 - \exp\left(-\frac{r_{jk}}{r_0}\right)\right]^2,$$

and comparable parameters $U_0$ and $r_0$.

The numerical experiment is organized as follows. The whole system is arranged with respect to the surface so that the distance separating it from the nearest segment be $r_0$; this segment, attracted by the surface, gradually drags out the remaining elements of the system behind it in accordance with the equations of motion $\partial r_j/\partial t = F^j$, where the total force includes all the system interactions: $F^j = F^j_{\mathrm{elastic}} + F^j_{\mathrm{VdW}} + F^j_{\mathrm{interact}}$. Little by little, the fibers undergo deformation as they are attracted to the surface and to one another and begin to pull with them the stiff rod of the base. The entire system turns, which not only makes it closer to the surface along the vertical axis but also pulls out the already attached fragments along the horizontal axis. This effect is especially apparent in a simplified two-dimensional (2D) model in which the motion occurs only in the $xz$ plane. In this case, all instantaneous positions of the fiber segments at discrete instants of time, as well as the trajectories of their contact points, can be depicted together on the plane. Such a picture for the typical scenario is presented in Fig. 16, where instantaneous positions and trajectories are shown by black and gray lines, respectively.

Rotation of the root rod is the key difference between this scenario and the ordinary attraction of a regular grid of vertical fibers to the surface. As is seen directly from Fig. 16, this rotation causes a pulling effect that *does not require active control* by the animal (or the artificial mechanism) but acts automatically owing to the structure of the system formed by natural selection. It was confirmed in earlier experiments and demonstrated theoretically that such a longitudinal displacement enhances adhesion of thin films [1, 24]. Importantly, in the course of this pulling process the spatulae attached to the surface gradually *turn oppositely to the direction of motion*. This rotation produces typical configurations that are clearly seen in SEM images of real gecko hairs gradually attaching to the surface (Fig. 2g), where spatulae are usually turned in the direction which is opposite to their original orientation (Fig. 3e, f).

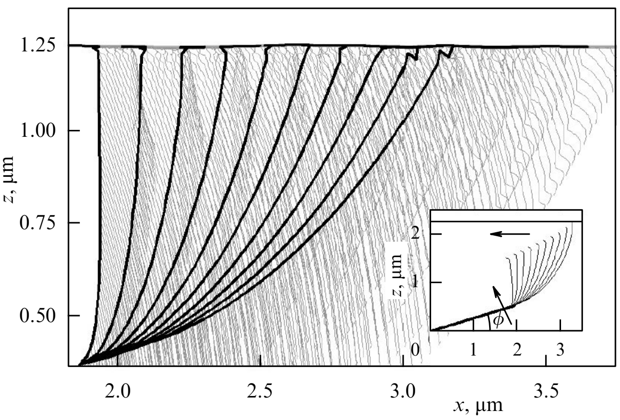


**Figure 16.** Behavior of the reduced model in $xz$ plane. The fibers and trajectories of segment contact points are shown by bold black and thin gray lines, respectively. Initial configuration is presented in the inset. The arrows show directions of the system motion, which appear owing to the joint action of attraction of the fibers to the surface and efficient pulling along the horizontal axis due to induced rotation.

The mutual shift of the spatula tips in the vertical direction prevents their clusterization after detachment from the surface. The structure was optimized by natural selection so that fibers reciprocally displaced in space release the elastic energy stored not only in horizontal but also in vertical directions, which facilitates their separation as they move away from the surface. On the other hand, a very strong vertical displacement at a fixed inclination angle $\varphi_0$ of the basal rod may result in certain fibers remaining very far from the surface and never coming in contact with it. This poses a formally mathematical problem of optimization. Its solution requires a comparison of the fiber structure behavior with and without mutual attraction between the fibers. To this effect, it is convenient to visualize the time-dependent fraction of attached fibers and angle $\varphi$, as well as their final values, depending on the different values of a vertical shift $\Delta$. In the case of noninteracting fibers, the results are quite trivial. Of course, the time-dependent behavior of angle $\varphi$ in this problem is readily predictable. As soon as the very first fiber attaches to the surface, the angle $\varphi$ starts to grow. The restoring force $f^\varphi = B(\varphi_0 - \varphi)$ works against this rotation and, in principle, stops the angle $\varphi$ rising at some steady-state value as $t \to \infty$. In this limit, the fibers whose tips are significantly shifted in the vertical direction remain unattached to the surface and do not participate in forming the total adhesive force. At the same time, the involvement of additional fibers in the contact increases the adhesive force and promotes the change in the final angle $\varphi$ as $t \to \infty$. Therefore, the result of this self-consistent problem depends on the totality of all forces that become involved in the process as it develops.

Quite a different picture appears when the fibers interact with each other. The system demonstrates a quite apparent optimum $\Delta$ depending on the shift magnitude, the main cause being that a very small shift promotes mutual attraction of the fibers suspended close to one another and descending synchronously; as a result, they gain the ability to build clusters before they approach the surface. Such clusterization impairs their ability to find a proper position on the surface and weakens the adhesive force. As before, in the limit when $\Delta \to \infty$, the interaction of the fibers becomes too weak and they behave almost as they do in the absence of interaction.

One of the important disadvantages of the two-dimensional model is that it fails to reproduce a distance between the spatulae in the $y$-direction orthogonal to the basal rod rotation plane $xz$. At the same time, the $y$-coordinate becomes extremely important when all fibers are in touch with the surface: first, because the attachment combined with rotation leads to a turn of the structure, which aligns all the spatulae in one direction, and second, because they formally overlap on the surface in two dimensions, which they do not experience in a real situation. This observation is well illustrated in Fig. 17 showing two different views of the

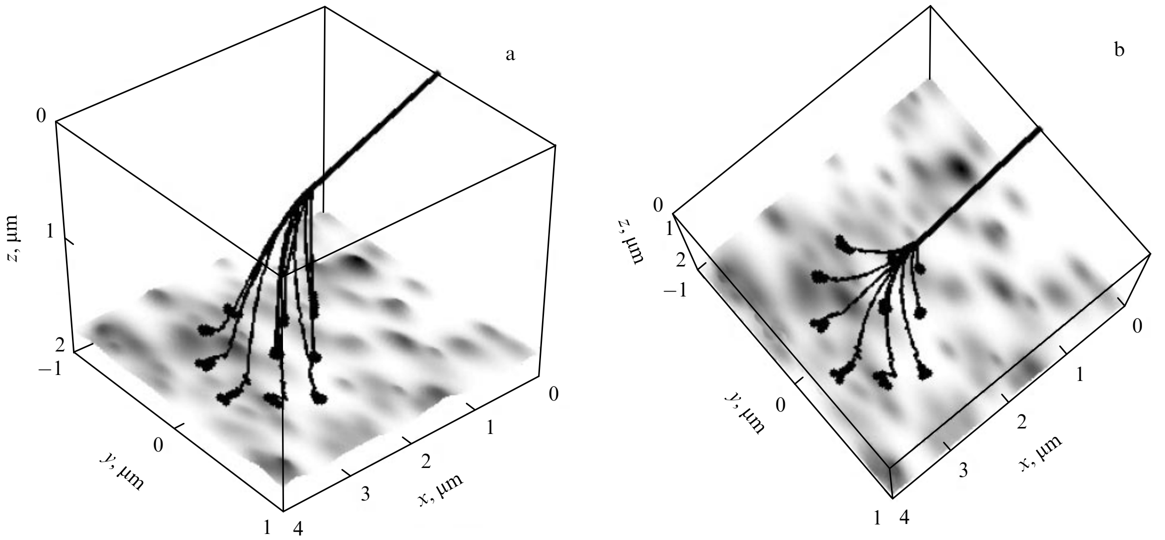


**Figure 17.** Two different views of the same configuration of the modelled system attached to the surface are shown in isometric (a) and almost vertical (b) projections, respectively. All symbols are the same as in Fig. 15.

same configuration of the modelled system attached to the surface in isometric (Fig. 17a) and almost vertical (Fig. 17b) projections.

The spatulae thus spaced rapidly return to the initial position after detachment from the surface. Certainly, this effect interferes with clusterization and together with hierarchical organization appears to greatly contribute to the efficiency of the natural system [51, 52]. At the same time, pulling effect improves contact in the attached state [24]. It should be emphasized that these effects are of a purely mechanical nature and do need regulation once the system is optimized either by natural selection or by modeling (in the case of artificial constructions).

## 6. Shear-induced adhesion: contact mechanics of biological spatula-involved systems

One of the many problems arising from the behavior of complicated adhesive systems and awaiting solution is the generation of spatula contact with a rough surface by a shear force when the spatula tip is not initially oriented along the surface. The present section is designed to discuss the following issues based on the numerical dynamic approach:

(1) What is the role of the thickness gradient in the process of contact formation?

(2) Does a shear improve contact?

(3) Is there an optimal distance or an optimal shear force improving contact?

To simulate shear-induced adhesion, we used the model configuration shown schematically in Fig. 18 presenting the two-dimensional projection of the system onto the vertical plane. Spatulae are considered to be elastic plates of variable thickness brought into contact with a rough surface at a certain angle $0 < \alpha < \pi/2$ and pulled out in the horizontal direction by force $F$.

As usual, attraction to the surface is due to the van der Waals force generated by potential $U_{\mathrm{VdW}}(r) = U_0[1 - \exp(-ar)]^2$, and the stiff contact surface is fractal. The adhesive force competes with resistance of the spatulae to bending. In accordance with the general theory of elasticity [62], the elastic energy of the flexible plate is given by the following integral:

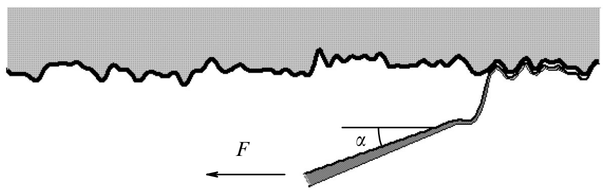


**Figure 18.** Conceptual diagram of the numerical model. A terminal part of the spatula is modelled by an elastic plate of variable thickness. It is brought into contact with the rigid rough surface at a certain angle $\alpha$ and pulled out in the horizontal direction by force $F$.

$$W_{\mathrm{elastic}} = \frac{E}{24(1-\nu^2)} \iint \mathrm{d}x\,\mathrm{d}y\, h^3(x,y) \left\{ \left( \frac{\partial^2 z}{\partial x^2} + \frac{\partial^2 z}{\partial y^2} \right)^2 + 2(1-\nu) \left[ \left( \frac{\partial^2 z}{\partial x\, \partial y} \right)^2 - \frac{\partial^2 z}{\partial x^2} \frac{\partial^2 z}{\partial y^2} \right] \right\}, \quad (17)$$

where $E$ is Young's modulus, $\nu$ is the Poisson ratio, and we put $\nu = 1/3$. The equation of motion has the form

$$\gamma \frac{\partial z(x,y)}{\partial t} = -\frac{\partial W_{\mathrm{elastic}}[z]}{\partial z} - \frac{\partial U_{\mathrm{VdW}}[z]}{\partial z}, \quad (18)$$

where $\gamma$ is the dissipation factor determining a characteristic time-scale of relaxation, $\gamma = 1$. The horizontal component of the van der Waals force $F^x_{\mathrm{VdW}} = -\partial U_{\mathrm{VdW}}(z(x))/\partial x$ competes with the external shear force $F^x$. When $F^x$ exceeds the total resistance of contact segments (in fact, merely distorted by force $F^x_{\mathrm{VdW}}$), one has $\int \mathrm{d}x\,\mathrm{d}y\, F^x_{\mathrm{VdW}} > |F^x|$, and the whole over-damped system begins to move in the horizontal direction with a speed given by the relation

$$\gamma \frac{\partial x}{\partial t} = F^x - \int \mathrm{d}x\,\mathrm{d}y\, F^x_{\mathrm{VdW}}. \quad (19)$$

Equations (18) and (19) make up a complete numerically solvable system. The typical instantaneous configuration of the system found numerically is shown in Fig. 19.

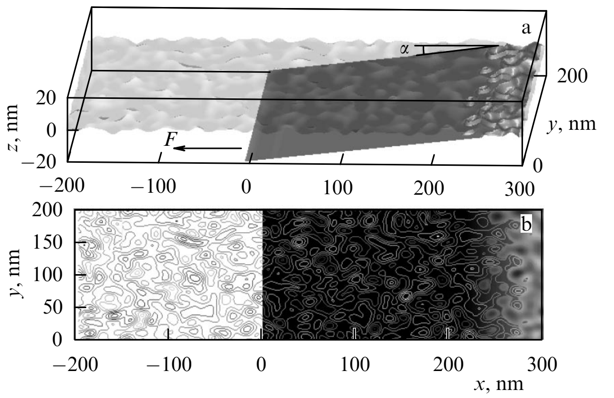


**Figure 19.** (a) Typical 3D configuration of an elastic plate obtained at an arbitrary time instant. Rigid 'ceiling' is shown by semitransparent light-gray upper surface. Instantaneous configuration of the flexible plate is presented by the grayscale map (darker color corresponds to the deeper values of the $z$-coordinate). (b) The picture is completed by a contour plot of a rough surface where instant contact areas shown by the grayscale map are seen directly.

In theory, it can be expected that the stronger the external force, the faster the rotating plate is attracted to the surface. However, if the external force exceeds a certain critical value, it may tear off the segments beginning to attach, which leads to their sliding; hence, the problem of optimization. To address it, we performed two sets of numerical simulations: one at a fixed initial inclination angle $\alpha$ and varying force $F$, and the other at a varying angle and fixed force. The results are summarized in Fig. 20.

The numerical experiments were organized as follows. The surface $Z(x, y)$ is generated as a numerical array $(500, 200)$ whereto an area of $500 \times 200$ nm corresponds, and the mobile plate has a size of $200 \times 200$ nm. It was verified that such a size of the array is large enough to provide good statistics for substantial self-averaging of the computable values. Then, one end of the plate is brought into contact with the surface at some trial angle $\alpha$ and left in this position for a certain transient time $t_0$, during which the real distribution of contact sites in this region is set up spontaneously ($t_0 \approx 2$ μs) at a zero external force, $F_{t<t_0} = 0$. At $t = t_0$, the pulling is turned on. The process is continued up to the maximum time ($t_{\max} = 10$ ms), which corresponds to the observed time for contact formation by the gecko footpad [46].

Figure 20 shows that different random realizations of the substrate surface $Z(x, y)$ manifest themselves either only in small deviations of values or, sometimes, in mutual intersections of qualitatively similar monotonic curves, but do not affect the general result. As expected, the higher force leads to a faster decrease in the inclination angle and to attraction of the plate to the surface till the force approaches the critical value, $F_{\text{crit}} \approx 20$ nN; thereafter, the weak horizontal drift $\delta x = x - x_0$ of the system from its starting position $x_0$ turns into fast sliding.

It seems natural that although an animal is unable to precisely optimize the horizontal pulling force, it can nonetheless control an approach of the total attachment force to a threshold value, after which a break occurs and some way or other maintain its strength close to this threshold without exceeding it. The critical force $F_{\text{crit}}$ depends on the initially attached region; consequently, $F_{\text{crit}}$ correlates with the initial inclination angle $\alpha$. Figure 20c shows the time dependences of the plate area contact fraction at a constant pulling force $F = 10$ nN and an angle varying within the $0.05\pi/2 \leqslant \alpha \leqslant 0.95\pi/2$ range. The arrow indicates an angle growth direction. Evidently, the pulling promotes attraction even at very small angles, i.e., the fraction of attached segments spontaneously increases even during the transient period $t < t_0$.

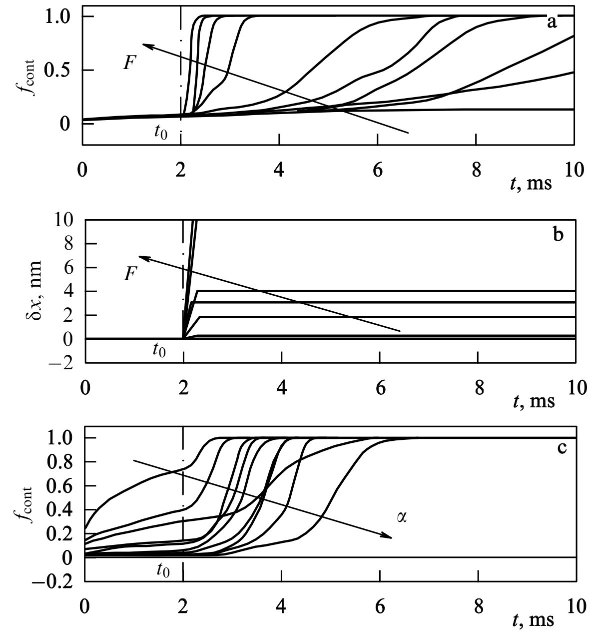


**Figure 20.** Time-dependent fraction $f_{\text{cont}}$ of the attached plate area normalized to its total area at different values of the pulling force and constant $\alpha = 0.2\pi$ (a) and the respective horizontal displacement $\delta x$ of the attached plate end (b). Arrows indicate the direction of external force growth. Bold lines fit dependences corresponding to forces $F = 22$ nN and $F = 20$ nN that exceed the critical force $F_{\text{crit}}$ at which continuous plate slippage occurs. The remaining curves correspond to the forces uniformly distributed within the $0 < F < F_{\text{crit}}$ interval. (c) The attached fraction of the plate area at a fixed pulling force $F = 10$ nN and variable angle $0.05\pi/2 \leqslant \alpha \leqslant 0.95\pi/2$. The arrow indicates an angle growth direction.

It can be concluded that horizontal pulling provides advantages over vertical load. It probably explains why most animals having hairy footpads make use, one way or another, of such horizontal pulling and have developed an adaptive trait in the form of spatula-shaped tips. The numerical experiment has demonstrated that this strategy is efficient in a wide range of forces and initial inclination angles of the spatulae with respect to the surface; therefore, it is highly resistant to variations of real conditions.

It can be supposed that artificial adhesives having tips in the form of a spatula will have advantages over isotropic mushroom-shaped structures. This feature, together with material thickness or stiffness gradients [72] and nontrivial fiber distribution in three-dimensional space [73], can be of special value for future biologically substantiated adhesive systems.

## 7. Conclusions

This review is concerned with the analysis of highly adhesive and friction-possessing biological microstructures with an accent placed on the methods of their numerical modeling and on the search for parameters determining optimal adhesion on surfaces of different topographies. The original simplest model was an array of vertically fixed fibers (setae) in contact with a rough surface. It was revealed by varying geometric and elastic properties of the fibers that there is an optimal elasticity, and as it turned out, in contrast to naive intuitive expectations, the fibers must be sufficiently stiff. The model was then extended by adding one more degree of freedom, namely deflection of the setae in the lateral direction with respect to the surface.

This degree of freedom allows the setae to adapt to the local surface topography: their distortion in the horizontal direction compensates the fractal structure in the vertical direction at different rough amplitudes, including large enough ones. The spatial redistribution of the setae has two essential consequences. First, perturbation of the uniform distribution markedly affects the process of film detachment from the surface, because many setae attach to one and the same surface asperity and detach almost simultaneously. Second, this effect may result in setal clusterization, because the fibers fail to separate after they leave the surface. The attachment of many fiber ends to the same asperities on the surface facilitates their mutual attraction and subsequent clusterization.

One of the methods to prevent clusterization is the introduction of setal stiffness gradients that evolved in many living creatures through natural selection. The influence of stiffness gradients has been thoroughly investigated in numerical experiments, in which it was shown that fibers that are highly stiff over their almost entire length and possess only relatively short soft ends have advantages over fibers with other possible combinations of these parameters.

Another approach to the prevention of clustering also ‘used’ in many biological structures consists in the creation of a hierarchical structure, i.e., 3D spatial distribution of the fibers in the form of distinctive bunches suspended from a common relatively stiff root. This option for enhancing the system’s efficiency was also considered in the framework of the numerical model. The spatially separated hairs rapidly return to the initial position after detachment from the surface, preventing clusterization and, together with the hierarchical structure, greatly contributing to the efficiency of natural systems by improving contact in the attached state.

One of the purely mechanical methods for optimizing adhesive properties is pulling that optimizes the hair distribution over the surface. The pulling effect is partially manifested even in the case of a strictly normal contact with the lateral hair motion. It is important from both biological and structural (applied) standpoints that this purely mechanical effect does not require regulation.

Finally, one of the models simulates the fiber end structure with a characteristic spatula that spontaneously formed over the course of convergent evolution in a variety of biological species using adhesive attachment to rough surfaces. The model takes into consideration the very apparent stiff gradient along the spatula.

The main problem in this context is to what extent the pulling effect improves spatula adaptation to the rough surface. It was revealed that horizontal pulling has certain advantages over vertical load. This probably explains why most animals having hairy footpads make use of this strategy one way or another and developed an adaptive trait in the form of spatula-shaped tips. Numerical experiments demonstrated that this approach is efficient in a wide range of forces and initial inclination angles of the plates to the surface; therefore, it is highly resistant to variations of real conditions. With this in mind, it can be speculated that artificial adhesives having tips in the form of a spatula will take advantages over isotropic mushroom-shaped structures [72, 73].

The data obtained can be used to develop new promising biologically substantiated adhesive systems.

## References

1. Autumn K et al. *Nature* **405** 681 (2000)
2. Autumn K et al. *Proc. Natl. Acad. Sci. USA* **99** 12252 (2002)
3. Cappella B, Dietler G *Surf. Sci. Rep.* **34** 1 (1999)
4. Persson B N J *J. Chem. Phys.* **118** 7614 (2003)
5. Persson B N J et al. *J. Phys. Condens. Matter* **17** R1 (2005)
6. Scherge M, Gorb S N *Biological Micro- and Nanotribology: Nature’s Solutions* (Berlin: Springer, 2001)
7. Sitti M, Fearing R S, Adhes J *J. Adhesion Sci. Technol.* **17** 1055 (2003)
8. Geim A K et al. *Nature Mater.* **2** 461 (2003)
9. Northen M T, Turner K L *Nanotechnology* **16** 1159 (2005)
10. Yurdumakan B et al. *Chem. Commun.* **2005**3799 (2005)
11. Persson B N J, Gorb S *J. Chem. Phys.* **119** 11437 (2003)
12. Campolo D, Jones S D, Fearing R S, in *IEEE Nano August 12–14, San Francisco* (2003)
13. Autumn K et al. *J. Exp. Biol.* **209** 3569 (2006)
14. Filippov A E, Popov V L *Phys. Lett. A* **358** 309 (2006)
15. Majidi C et al. *Phys. Rev. Lett.* **97** 076103 (2006)
16. Filippov A E, Popov V *J. Phys. Condens. Matter A* **19** 096012 (2007)
17. Gorb S *Attachment Devices of Insect Cuticle* (Dordrecht: Kluwer Acad. Publ., 2001)
18. Gorb S N, Beutel R G *Naturwissenschaften* **88** 530 (2001)
19. Gorb S N et al. *Integr. Comp. Biol.* **42** 1127 (2002)
20. Creton C, Gorb S N *MRS Bull.* **32** 466 (2007)
21. Voigt D, Schuppert J M, Dattinger S, Gorb S N *J. Insect Physiol.* **54** 765 (2008)
22. Hui C Y et al. *J. R. Soc. Interface* **1** 35 (2004)
23. Varenberg M, Pugno N M, Gorb S N *Soft Matter* **6** 3269 (2010)
24. Filippov A E, Popov V L, Gorb S N *J. Theor. Biol.* **276** 126 (2011)
25. Borodich F M, Gorb E V, Gorb S N *Appl. Phys. A* **100** 63 (2010)
26. Jagota A, Bennison S J *Integr. Comp. Biol.* **42** 1140 (2002)
27. Spolenak R, Gorb S N, Arzt E *Acta Biomater.* **1** 5 (2005)
28. Peisker H, Michels J, Gorb S N *Nature Commun.* **4** 1661(2013)
29. Weis-Fogh T *J. Exp. Biol.* **37** 889 (1960)
30. Weis-Fogh T *J. Mol. Biol.* **3** 648 (1961)
31. Michels J, Gorb S N *J. Microsc.* **245** 1 (2012)
32. Gorb S, Varenberg M, Peressadko A, Tuma J *J. R. Soc. Interface* **4** (13) 271 (2007)
33. Vincent J F V *Composites A* **33** 1311 (2002)
34. Barbakadze N, Enders S, Gorb S, Arzt E *J. Exp. Biol.* **209** 722 (2006)
35. Klein M-C, Deuschle J, Gorb S *J. Comp. Physiol. A* **196** 659 (2010)
36. Wang R Z, Weiner S *J. Biomech.* **31** 135 (1997)
37. Fong H et al. *Mater. Sci. Eng. C* **7** 119 (2000)
38. Perez Goodwyn P et al. *J. Comp. Physiol. A* **192** 1233 (2006)
39. Gorb S N “Smooth attachment devices in insects”, in *Advances in Insect Physiology: Insect Mechanics and Control* (Eds J Casas, S J Simpson) (London: Elsevier, 2008) p. 81
40. Jagota A, Bennison S J *Integr. Comp. Biol.* **42** 1140 (2002)
41. Hiller U *Z. Morphol. Tiere* **62** 307 (1969)
42. Huber G, Gorb S N, Spolenak R, Arzt E *Biol. Lett.* **1** 2 (2005)
43. Arzt E, Gorb S, Spolenak R *Proc. Natl. Acad. Sci. USA* **100** 10603 (2003)
44. Schargott M *Bioinspir. Biomim.* **4** 026002 (2009)
45. Varenberg M, Pugno N M, Gorb S N *Soft Matter* **6** 3269 (2010)
46. Gao H, Yao H *Proc. Natl. Acad. Sci. USA* **101** 7851 (2004)
47. Spolenak R, Gorb S, Arzt E *Acta Biomater.* **1** 5 (2005)
48. Jagota A, Bennison S J *Integr. Comp. Biol.* **42** 1140 (2002)
49. Sameoto D, Menon C *Smart Mater. Struct.* **19** 103001 (2010)
50. Yurdumakan B et al. *Chem. Commun.* **2005** 3799 (2005)
51. Kim T W, Bhushan B *Ultramicroscopy* **107** 902 (2007)
52. Bhushan B, Peressadko A G, Kim T W *J. Adhes. Sci. Tech.* **20** 1475 (2006)
53. Stork N E *Zool. J. Linn. Soc.* **68** 173 (1980)
54. Stork N E *J. Natl. Hist.* **17** 583 (1983)
55. Gorb S N *Proc. R. Soc. London B* **265** 747 (1998)

56. Gorb S N *Attachment Devices of Insect Cuticle* (Dordrecht: Kluwer Acad. Publ., 2001)
57. Tian Y et al. *Proc. Natl. Acad. Sci. USA* **103** 19320 (2006)
58. Niederegger S, Gorb S N *J. Insect Physiol.* **49** 611 (2003)
59. Niederegger S, Gorb S N *J. Comp. Physiol. A* **192** 1223 (2006)
60. Eimüller T, Guttmann P, Gorb S N *J. Exp. Biol.* **211** 1958 (2008)
61. Kendall K *J. Phys. D* **8** 1449 (1975)
62. Landau L D, Lifshitz E M *Theory of Elasticity* 2nd ed. (Oxford: Pergamon Press, 1981)
63. Popov V L *Contact Mechanics and Friction*: *Physical Principles and Applications* (Heidelberg: Springer, 2010)
64. Schargott M, Popov V, Gorb S *J. Theor. Biol.* **243** 48 (2006)
65. Huber G et al. *Proc. Natl. Acad. Sci. USA* **102** 16293 (2005)
66. Kim S, Aksak B, Sitti M *Appl. Phys. Lett.* **91** 221913 (2007)
67. Kim S, Sitti M *Appl. Phys. Lett.* **89** 261911 (2006)
68. Kim S et al. *IEEE Nano* **08** 780 (2008)
69. Kim T W, Bhushan B *J. Adhesion Sci. Technol.* **21** 1 (2007)
70. Murphy M P, Aksak B, Sitti M *J. Adhesion Sci. Technol.* **21** 1281 (2007)
71. Chen B, Wu P D, Gao H *J. R. Soc. Interface* **6** 529 (2009)
72. Filippov A E, Gorb S N *Beilstein J. Nanotechnol.* **5** 837 (2014)
73. Filippov A E, Gorb S N *Interface Focus* **5** 20140065 (2015)